Annals of Biomedical Engineering, Vol. 32, No. 7, July 2004 (©2004) pp. 932–946

Characterization of the Atherosclerotic Carotid Bifurcation Using MRI, Finite Element Modeling, and Histology

M. R. KAAZEMPUR-MOFRAD,[1,5*] A. G. ISASI,[1*] H. F. YOUNIS,[1*] R. C. CHAN,[2] D. P. HINTON,[2]
G. SUKHOVA,[3] G. M. LAMURAGLIA,[4] R. T. LEE,[3] and R. D. KAMM[1]

[1]Department of Mechanical Engineering and Biological Engineering Division, Massachusetts Institute of Technology, Cambridge, MA; [2]Department of Radiology, Massachusetts General Hospital, Harvard Medical School, Boston, MA; [3]Department of Cardiovascular Medicine, Brigham & Women's Hospital, Harvard Medical School, Boston, MA; [4]Department of Vascular Medicine, Massachusetts General Hospital, Harvard Medical School, Boston, MA; and [5]Department of Surgery, Massachusetts General Hospital, Harvard Medical School, Boston, MA

(Received 4 September 2003; accepted 19 February 2004)

Abstract—Atherogenesis is known to be associated with the stresses that act on or within the arterial wall. Still, the uneven distribution of atherosclerotic lesions and the impact of vessel remodeling on disease progression are poorly understood. A methodology is proposed to study the correlations between fluid dynamic parameters and histological markers of atherosclerosis. Trends suggested by preliminary data from four patients with advanced carotid bifurcation arterial disease are examined and compared to hypotheses in the literature. Four patients were scanned using MRI and ultrasound, and subsequently underwent carotid endarterectomy. For each patient, a geometric model and a numerical mesh were constructed from MR data, and velocity boundary conditions established. Computations yield values for average wall shear stress (WSS), maximum wall shear stress temporal gradient (WSSTG), and Oscillatory Shear Index (OSI). Following surgery, the excised plaques were sectioned, stained for smooth muscle cells (SMC), macrophages (Mϕ), lipid (LIP), and collagen (COL), and analyzed quantitatively. Correlations attempted between the various fluid dynamic variables and the biological markers were interesting but inconclusive. Tendencies of WSSTG and WSS to correlate negatively with Mϕ and LIP, and positively with COL and SMC, as well as tendencies of OSI to correlate positively with Mϕ and LIP and negatively with COL and SMC, were observed. These trends agree with hypotheses in the literature, which are based on *ex vivo* and *in vitro* experimental studies.

Keywords—Atherosclerosis, MRI, FEM, Carotid 3D geometry, Low/oscillatory shear stress, Excised plaque composition.

INTRODUCTION

Atherosclerosis is responsible for two thirds of all deaths.[1] Even though several systemic risk factors have been identified, these fail to fully explain the uneven distribution of atherosclerotic lesions within the arterial tree. Atherosclerosis is a geometrically focal inflammatory disease, preferentially affecting sites of complex hemodynamics, such as bifurcations, junctions, and regions of high curvature.[5] These observations, in combination with results from *in vitro* studies that show a strong influence of fluid dynamic shear on cell function,[36] have led to the hypothesis that disease progression is related to stresses acting on vascular cells.

Current understanding of the role of hemodynamic stress in the development and progression of atherosclerosis is incomplete. Stresses that act on or within the arterial wall affect the inflammatory process, as well as the heterogeneous remodeling of vessel structure and composition.[6] In the early stages of disease, low or oscillatory fluid shear stresses cause monocyte adhesion and affect endothelial cell function, while high cyclical mechanical strain affects endothelial and smooth muscle cell activity.[17,34] In the late stages of atherosclerosis, low or oscillatory fluid shear stress correlates with vulnerable areas in the atherosclerotic plaque, such as sites with significant lipid deposition,[8] relative smooth muscle cell depletion,[12] increased collagenolysis,[33] and macrophage accumulation,[12,22] all characteristic of the inflammatory/remodeling process. High mechanical strain enhances matrix metalloproteinase (MMP) production by macrophages, a factor that could contribute to weakening of the plaque cap.[21]

Computational studies[11,15,35] suggest that mass transport also plays a role in atherogenesis. Zones of hypoxia (low oxygen transport from blood to wall) and elevated LDL have been shown to colocalize. Such zones have been shown to correspond to areas of atherosclerotic lesion development and/or intimal thickening. Deng *et al*.[8] showed that the efflux rates of lipids and their breakdown products from the vessel walls were suppressed in the region of disturbed flow, with slow circulation distal to stenoses. Their model predicts that locally disturbed blood flow at arterial stenoses and arterial anastomoses provide favorable conditions for

---

Address correspondence to Roger D. Kamm, 77 Massachusetts Avenue, Room NE47-321, Cambridge, MA 02139. Electronic mail: rdkamm@mit.edu

*Each contributed equally to this paper.

lipid infiltration into vessel walls while also impairing the release into the blood of atherogenic substances accumulated in the vessel wall. Falk[12] have shown that ruptured fibrous caps have twice as many macrophages as unruptured fibrous caps and half as many smooth muscle cells. Therefore, while inflammation and matrix degradation decrease plaque strength, inadequate numbers of smooth muscle cells may be present to repair the degradation. Sukhova *et al.*[33] demonstrated that atheromatous rather than fibrous plaques are likely prone to rupture due to increased collagenolysis associated with macrophages, probably mediated by the interstitial collagenases MMP-1 and MMP-13.

Previous studies have shown that regions of low or oscillatory shear stress cause monocyte adhesion to the endothelial wall.[23] Low shear stress leads to the expression of VCAM-1, a monocyte adhesion molecule,[13] increased and prolonged NF-κB activity, a regulator of some endothelial cell adhesion molecules[25] and a reduction in nitric oxide (NO) release (augmented levels inhibit monocyte adhesion).[37,38] While extensive numerical work has identified regions of low shear stress for stenosed arteries, healthy and diseased bifurcations, to our knowledge, none have rigorously tested the validity of the low shear stress hypothesis by using *in vivo* data and correlating the resulting shear stress distributions to histology. Berger and Jou[2] summarize the work conducted to date on fluid mechanic modeling of steady and unsteady three-dimensional (3D) flows in stenotic vessels. Of these, however, only Stroud[32] used realistic geometries to represent the diseased arterial wall. Recently, Steinman *et al.*[31] examined the relationship between local hemodynamics and wall thickness using three realistic geometries, and found no quantitative general relationship between wall shear stress and wall thickness. Dirksen *et al.*[9] showed that the distribution of smooth muscle cells and macrophages relate to the *direction* of flow, but they did not calculate, nor compare their results to, detailed wall shear stress distributions.

Here we describe methods to generate, from MRI and ultrasound measurements *in vivo*, arterial geometrical models and velocity profiles for particular patients that are in turn used to calculate detailed blood flow and shear stress distributions. Specimens obtained from these same patients following endarterectomy are examined histologically to identify regions containing smooth muscle cells, lipid, macrophages, and collagen. A comparison is made on the basis of the hypothesis that this two-pronged approach can lead to a better appreciation of the role of hemodynamics in the progression of late stage arterial disease.

MATERIALS AND METHODS

MR Imaging

Four patients (ages 61–73) scheduled to undergo carotid endarterectomy (P1, P2, P3, and P4) were studied. The 2D MR images were obtained using a Siemens Sonata 1.5 Tesla system at the Massachusetts General Hospital NMR Center. The 2D MR images are perpendicular to a direction that is approximately aligned with the longitudinal axis of the patient's carotid bifurcation, as determined by the MR scanner operator following a series of scouting images. A localized 4-in. receiver surface coil for unilateral imaging was positioned over the carotid bifurcation to obtain images, 256 × 256 pixels in size, with in-plane resolution of approximately 0.39 mm. The slice thickness of these images was 2 mm. A black-blood spin-echo sequence[10,30] proton density weighting and fat suppression was used for ECG-gated acquisition of 20 slices through the carotid (2 cm below to 2 cm above the carotid bifurcation, see Fig. 1). The total MR scanning procedure required approximately 1 h. Centerline velocities at the planes of inlet and outlet of the carotid bifurcation were measured using ultrasound (Fig. 1).

Extraction of Inner and Outer Wall Coordinates

The inner arterial boundary at the lumen-intima interface and the outer arterial boundary at the adventitia-adjacent tissue interface are extracted with a multistep segmentation method originally developed for arterial wall measurement from B-mode ultrasound data.[4] An edge image and a smoothed image are jointly estimated from noisy MR data by minimization of a modified Mumford-Shah variational energy functional.[3] The geometry as presented

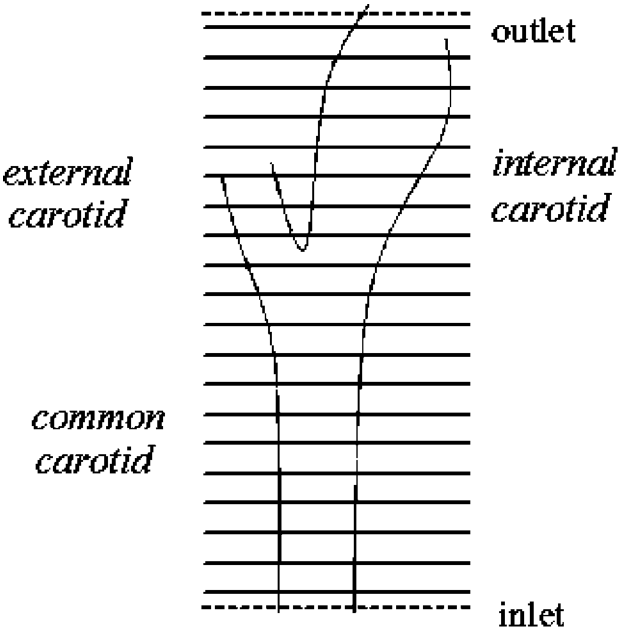

FIGURE 1. Sketch (not to scale) of MR geometry and ultrasound velocity data acquisition. The volume between any two adjacent solid horizontal lines represents the imaged region. Centerline velocities were measured using ultrasound at the inlet and outlet planes (dotted lines).

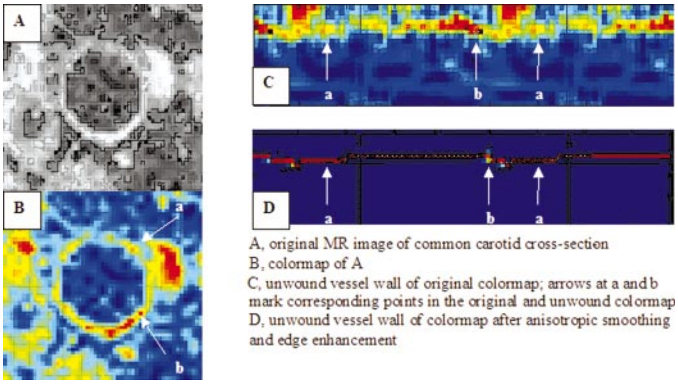

A, original MR image of common carotid cross-section
B, colormap of A
C, unwound vessel wall of original colormap; arrows at a and b mark corresponding points in the original and unwound colormap
D, unwound vessel wall of colormap after anisotropic smoothing and edge enhancement

FIGURE 2. Example of anisotropic smoothing and edge enhancement for an MR image of the common carotid.

corresponds to the diastolic pressure. This nonlinear processing step produces anisotropic smoothing of the raw data and image edge enhancement in a directionally sensitive manner (intensity gradients are enhanced at edges that correspond to a prior model of vessel boundaries having circumferential orientation). Curve evolution with deformable splines is then applied to the estimated edge field for final extraction of the inner and outer vessel walls. A deformable spline converts 2D data points into a useful curve representation: one starts with a simple curve and progressively deforms it into a shape which is able to approximate the data points within a given tolerance, by minimizing the "energy" of a deformable surface in an external potential field.[18] This procedure is illustrated in Fig. 2.

3D Reconstruction of the Carotid Bifurcation Geometry

The curves resulting from the method described above were transferred to the modeling software Solidworks$^{\mathrm{TM}}$ (SolidWorks Corporation, Concord, MA), where a base loft function interpolates across the 2D cross-sectional structures of each level of carotid bifurcation in order to yield 3D structures. The solid that results from interpolating across the outer contours produces the external 3D solid body, while the 3D structure that results from interpolating across the inner contours produces the 3D fluid volume. Next, the fluid volume is subtracted from the external volume, hollowing out the 3D outer wall solid body and yielding the arterial wall 3D solid structure [Fig. 3(b)], which is used later in matching the histological slice location to the histology specimen. No discernable differences in the 3D geometry were observed when lofting was repeated through the same series of 2D vessel cross-sections.

Constructing a 3D model from MR data comprises three basic steps: data acquisition, image segmentation, and construction of the 3D model itself from 2D curves. Each step has its sources of geometric errors and distortions. With respect to the resolution and image quality of the scanner, images that were 256 × 256 pixels in size, with in-plane

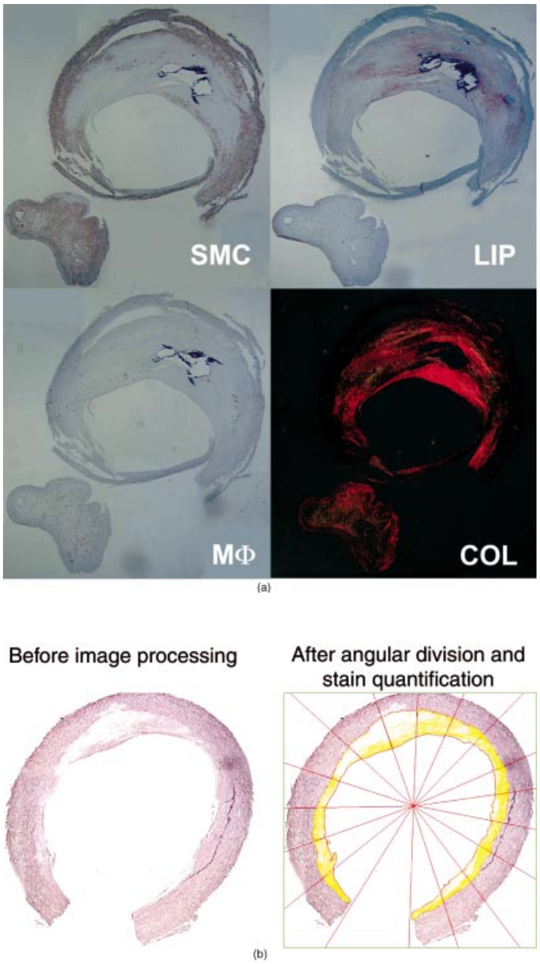

FIGURE 5. (a) Stains for COL, LIP, Mϕ, and SMC corresponding to slice 5 of P1, showing both internal (larger) and external (smaller) carotid cross sections. The reagent used in each of the four cases stains red the component in question. Each picture is taken from a position downstream to the cutting plane. The collagen image has a black background, since it is taken through a polarizing filter. (b) Subdivision of a specimen stained for SMC (slice 3 of P1: distal to the common carotid, immediately proximal to the bifurcation) into 16 equiangular segments and recognition (in yellow), of the area per segment that is stained in red.

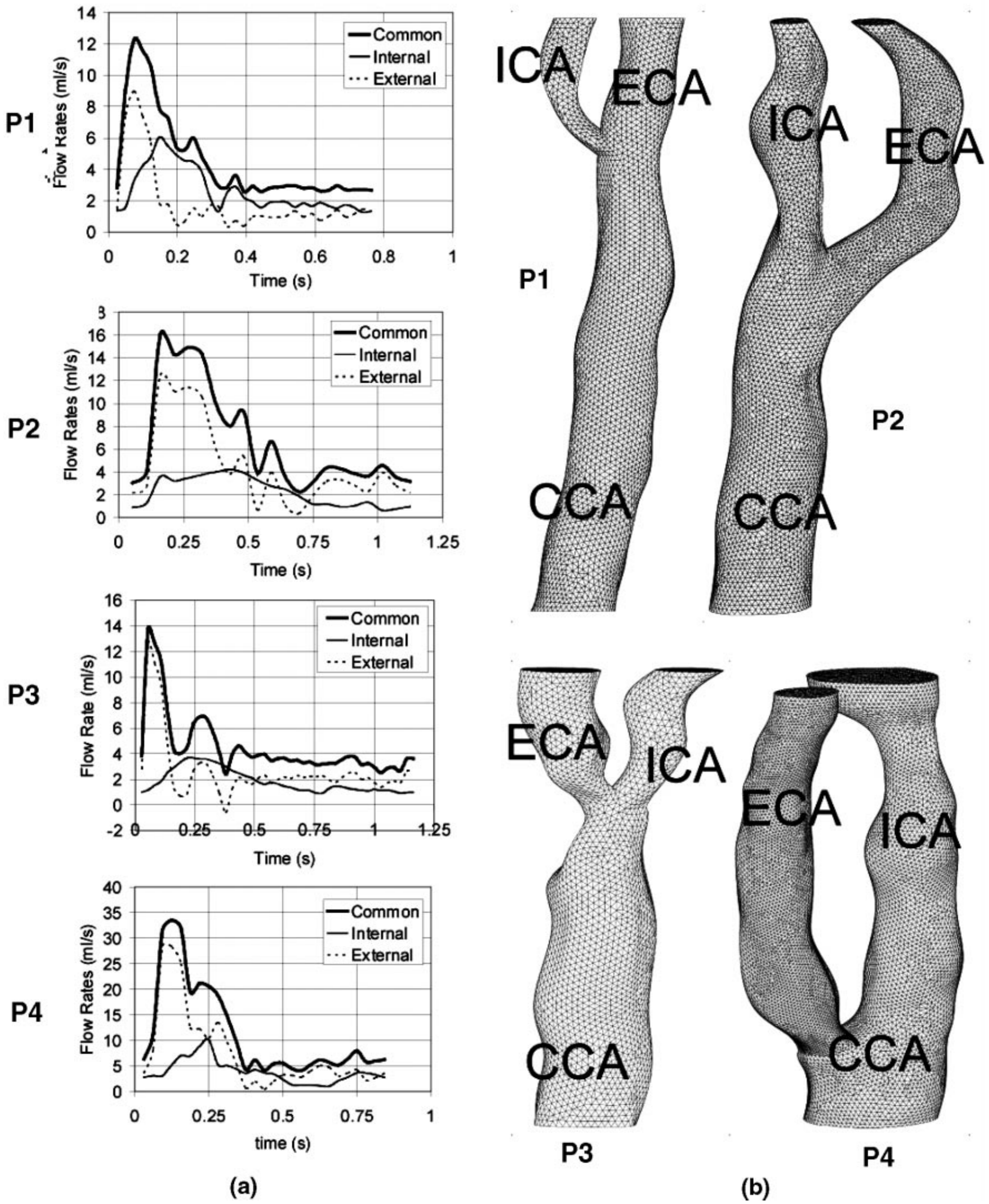

FIGURE 3. (a) Flow rate profiles for the common (bold), internal (plain), and external (dashed) carotid arteries during the cardiac cycle for P1–P4, generated using ultrasound centerline velocity measurements as a function of time. Flow rate in the external carotid is computed by subtracting internal carotid flow rate from common carotid flow rate. (b) FEM meshes for P1–P4 generated using linear element free meshing with an element edge size of 0.4 mm. CCA, ICA, and ECA denote the common, internal, and external carotids, respectively.

resolution of approximately 0.39 mm and slice thickness of 2 mm, were obtained for all four studied subjects. The average outer diameter for the four patients was about 10 mm, leading to errors of ±1 pixel signifying a ±4% error in one dimension. With respect to the segmentation, there is the possibility of the procedure yielding curves that are overly tortuous or overly smooth, given a certain tolerance in the energy minimizing function, leading to distortion and shrinkage of the geometry. Approximating the carotid cross sections as circumferences and the 3D slices as cylinders, this ±4% error in one dimension, Δr, would be transmitted into the 2D curves and the 3D final model, as $2\pi r(\Delta r)/\pi r^2$ and $2\pi r(\Delta r)h/\pi r^2 h$, respectively, that is, a ±8% error both in the area and the volume, at each axial position, where r is the average radius at a given axial position and h is the slice thickness. The same user segmented the MR data of all four patients, in an attempt to make the likelihood of such errors similar in all four data sets. Shrinkage and distortion can also occur at the 3D reconstruction step, but these errors are considered in general smaller than those of the first two steps. Once again, the same user performed the 3D reconstruction of the segmented data of all four subjects in an attempt to make the likelihood of such errors similar in all four datasets.

With respect to using MRI-based models as opposed to *ex vivo* preparations, a study of the aorto-iliac region of rabbits by Moore *et al*., showed substantial differences between these methods.[26] Bifurcation angles tended to be consistently larger in postmortem specimens, and vessel dimensions were consistently smaller in pressure-fixed specimens. *In vivo* MRI-based models underpredicted aortic dimensions immediately proximal to the bifurcation, causing appreciable variation in the aorto-iliac parent/child area ratio. This had an important effect on wall shear stress and separation patterns on the "hips" of the bifurcation, with mean wall shear stress differences ranging from 15 to 35%, depending on the model. Hence, *in vivo* MRI is thought to best replicate overall vessel geometry (vessel paths and bifurcation angle), while vascular casting seems to better capture detailed vessel cross-sectional dimensions and shape. Therefore, for the purposes of the present study, it is important to accurately characterize the local carotid bifurcation geometry when studying *in vivo* bifurcation hemodynamics.

Construction of the Finite Element Model (FEM) and Generation of the Flow Profiles

The resulting geometric model is imported into the FEM software (ADINA$^{\text{TM}}$), where a mesh is constructed that matches the vessel geometry, and the nodes on the inlet plane to the carotid bifurcation (common carotid, CCA), and those on one of the outlet planes to the carotid bifurcation (internal carotid, ICA, and external carotid, ECA) are extracted. Coordinates of these nodes are entered as arguments into a function[14] that generates a fully developed Womersley-type flow based on the ultrasound centerline velocity measurements [see, Fig. 3(a)]. Flow rate in the ECA is computed by subtracting the ICA flow rate from the CCA flow rate to ensure mass conservation.

Measured flow rates in the ECA were not used since, distal to the bifurcation where the domain of the MR-generated image ends and the velocity boundary conditions need to be applied, several smaller vessels that are difficult to image have branched off from the external carotid. Note that this procedure overestimates flow in the ECA. This has been previously shown, however, to have a minimal effect on hemodynamics in the carotid bulb, the region of most relevance to atherogenesis, but could influence the details elsewhere, particularly in the ECA.[40] The flow waveforms in the ICA are consistent with similar measurements reported in the literature.[31,41]

Finite Element Analysis and Application of Boundary and Initial Conditions

The simulations employ a finite element analysis software package (ADINA$^{\text{TM}}$, version 7.4, Automatic Dynamic Incremental Nonlinear Analysis, Watertown, MA). ADINA performs finite element analyses of structures, fluids, and fluid flows with structural interactions, having solid modeling capabilities and allowing for direct integration with other Parasolid-based CAD systems. In an earlier phase of this study we performed validation studies of ADINA flow and solid mechanics calculations[16] by using an idealized geometry similar to that of Delfino *et al*.[7]

Blood is treated as an incompressible, Newtonian fluid (an assumption that has repeatedly been shown to hold well for large arteries,[2,28] where shear rates generally exceed 100 s^{-1}) with a viscosity of 0.004 Pa·s and density of 1100.0 $\text{kg}\cdot\text{m}^{-3}$ and the flow assumed laminar.[19] The more severe constrictions could certainly cause turbulence, but the turbulence intensity is likely to be small. The vessel is assumed rigid on the assumption that the presence of plaque in these thickened, diseased arteries minimizes strains.[39] Unstructured meshing using four-node linear elements was used due to the complexity of the geometries involved. A grid sensitivity analysis was performed to ensure mesh independence of the WSS patterns, in particular at the throat of stenoses. The finest mesh which showed a ~4% uncertainty in stenosis WSS obtained with an element edge size of 0.4 mm [Fig. 3(b)]. The relative positions of the ECA and ICA of each patient were determined by establishing the presence of several smaller vessels branching off from the ECA downstream from the carotid bifurcation. In Fig. 3(b), the view of the reconstructed model was chosen so as to best depict the particular details of the geometry of each patient.

The rigid-walled fluid simulations were solved separately in two steps, using fully developed Womersley-type flow velocity boundary conditions. In the first step, a Womersley-type velocity profile corresponding to the centerline fluid velocity in the CCA and ICA was imposed on the respective arteries, while the ECA was left at zero traction. Flow profiles at the output of the ECA at the end of this step were then used as an input boundary condition to the second computational step, while retaining the Womersley flow at the CCA and imposing a traction-free boundary condition at the ICA. This second step was then considered the final computed solution as in Perktold *et al*.[28] To

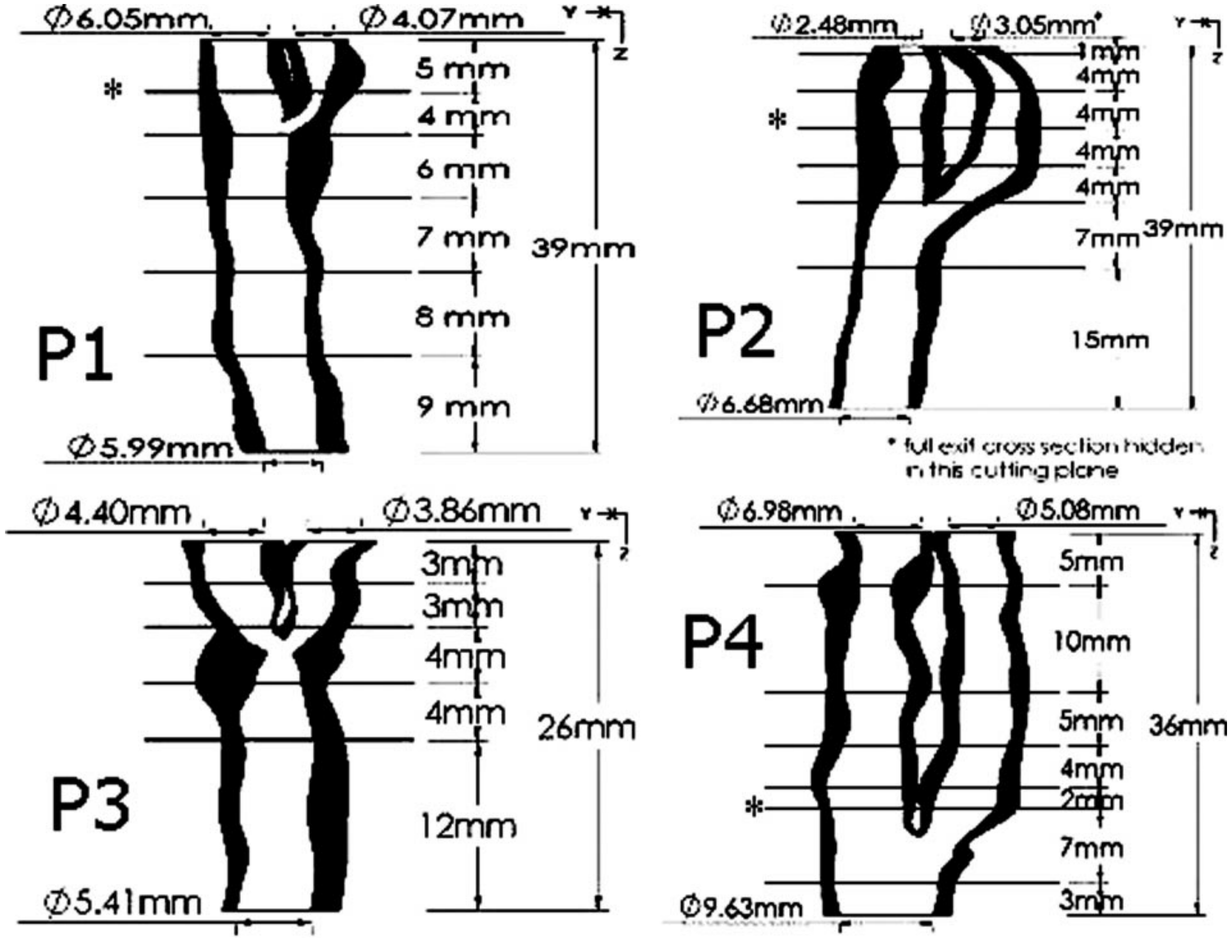

FIGURE 4. Location of the histology sections studied for each of the four patients.

achieve a periodic solution, the flow computation was allowed to run over two heart cycles, saving only the second one. All computations were performed using a SGI Origin 2000 equipped with four processors and 6 GB of RAM. Solution times varied between 12 and 24 h.

Excised Plaque Orientation

Following endarterectomy, the excised plaque specimens were collected and preserved in cold saline. Plaque angular orientation is tracked by observing the location of the surgical incision, which is assigned a reference value of zero degrees, and runs down the centerline of the carotid bulb–CCA interface. Because of the absence of the incision in the ECA, its angular orientation is unknown; all associations with fluid dynamic parameters herein are therefore solely of the CCA and ICA.

Processing of the Endarterectomy Specimens for Histology and Immunohistochemistry

Each specimen was processed within 1–2 h after surgery. Tissue sample was cut transversally in rings ranging between 2.5 and 4 mm in length (Fig. 4). Transverse sections of the reconstructed models were taken at the positions where the excised specimen was cut. Figure 4 reports the diameters for each transverse section of the models, as measured to an accuracy of 10 μm using the measuring tool in Solidworks$^{\text{TM}}$. Most analyzed cross sections were approximately circular, and the reported diameter corresponds to the length of the chord that most likely represents the section's diameter, as determined by the software user. The axial lengths shown in the figure were measured in the unloaded state. Each ring was embedded in optimal cutting compound, snap frozen in isopentaine precooled in liquid Nitrogen, and stored at -80°C. Acetone fixed 6 μm sections were stained for interstitial collagen (0.1% solution of Sirius Red F3BA in saturated aqueous picric acid), lipids (0.5% oil red O staining), smooth muscle cells (SMC, HHF-35 monoclonal anti-α-actin antibody), and macrophages (Mϕ, CD68 monoclonal antibody). For immunohistochemistry, we used avidin–biotin–peroxidase method (Universal Dako kit, DAKO Co., Carpinteria, CA), the reaction was visualized (brown-red end product) by 3-amino-9-ethyl carbazole (DAKO) [Fig. 5(a)].

Excised Plaque Composition Quantification

Once stained, each specimen was photographed, digitized, and imported into a commercial image processing software, OPTIMAS^{TM} for quantitative analysis. Each slice was divided into 16 equiangular segments over which the area of each histological variable (LIP, COL, SMC, and Mϕ) being examined *over the intimal layer* of the section was recognized in yellow and recorded. The intimal layer was determined as per the expertise of the histopathologist who collaborated in this study. The total area of the intimal layer of each equiangular segment was also recorded. For each equiangular segment, the yellow area was divided by the total intimal area, yielding the fractional composition of each histological variable at each of the 16 locations [see e.g., Fig. 5(b)].

Regression Analysis

The fractional areas for each histological variable were correlated against each of three hemodynamic parameters: the time-average wall shear stress (WSS), the maximum value during a complete cardiac cycle of the wall shear stress temporal gradient (WSSTG), and the Oscillatory Shear Index (OSI), defined later, each averaged per 22.5° segments (and 1 mm thickness; 0.5 mm above and 0.5 mm below the selected slice or cutting plane) and calculated from the finite element simulations. A finite thickness was assigned to each section to facilitate extraction of finite element data.

WSS was obtained by averaging the magnitude of the instantaneous wall shear stress vector over time (the entire cycle). Flow is 3D, so WSS is a two-component vector at each time. WSSTG was calculated by computing the gradient in the instantaneous wall shear stress between every two consecutive time points during the cycle, and taking the maximum of these values. OSI was calculated following the definition of Ku *et al.*[20]:

$$\mathrm{OSI} = \frac{\int_0^T |\vec{\tau}^*|\, dt}{\int_0^T |\vec{\tau}_\mathrm{w}|\, dt} \tag{1}$$

where $\vec{\tau}_\mathrm{w}$ is the instantaneous wall shear stress vector and $\vec{\tau}^*$ is the wall shear stress component acting in the direction opposite to the temporal mean wall shear stress vector.

As the data are not normally distributed, the Spearman rank order correlation coefficient and its corresponding significance test[29] were used in evaluating the correlations between each pair of variables (one hemodynamic parameter and one chemical component, respectively) around the circumference, for a particular axial position z. Only those correlations with $P < 0.05$ were considered conclusive.

RESULTS

Wall Shear Stress and Oscillatory Shear Index Patterns

Typical hemodynamic parameter bandplots and cutting planes for patients P_1–P_4 are shown in Fig. 6. Both P1 and P3 have severely stenosed ICA [Fig. 3(b)], however P1 has a much less severe stenosis in the ECA than P3. Wall shear stress throughout P1's ICA stenosis exceeds 10 Pa in most of the branch, since the stenosis is severe and long. In P3, shear stress in both throats of the ICA and ECA at the stenosis exceeds 10 Pa, but then decreases rapidly due to the dilation of the arteries immediately distal to the stenoses. Shear stress levels are generally less than 10 Pa in P2 and P4, even in the

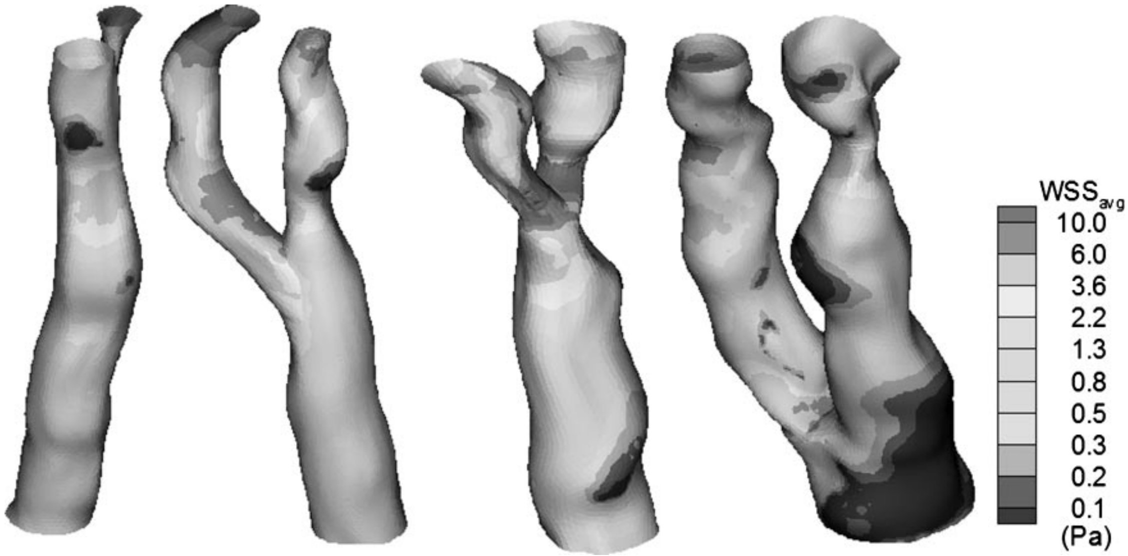

FIGURE 6. Computed average wall shear stress (WSS [Pa]), maximum wall shear stress temporal gradient (WSSTG [Pa/s]), and oscillatory shear index (OSI, dimensionless) profiles over the cardiac cycle for patient model P2. A logarithmic scale is used for WSS, in order to exaggerate regions of low average wall shear stress.

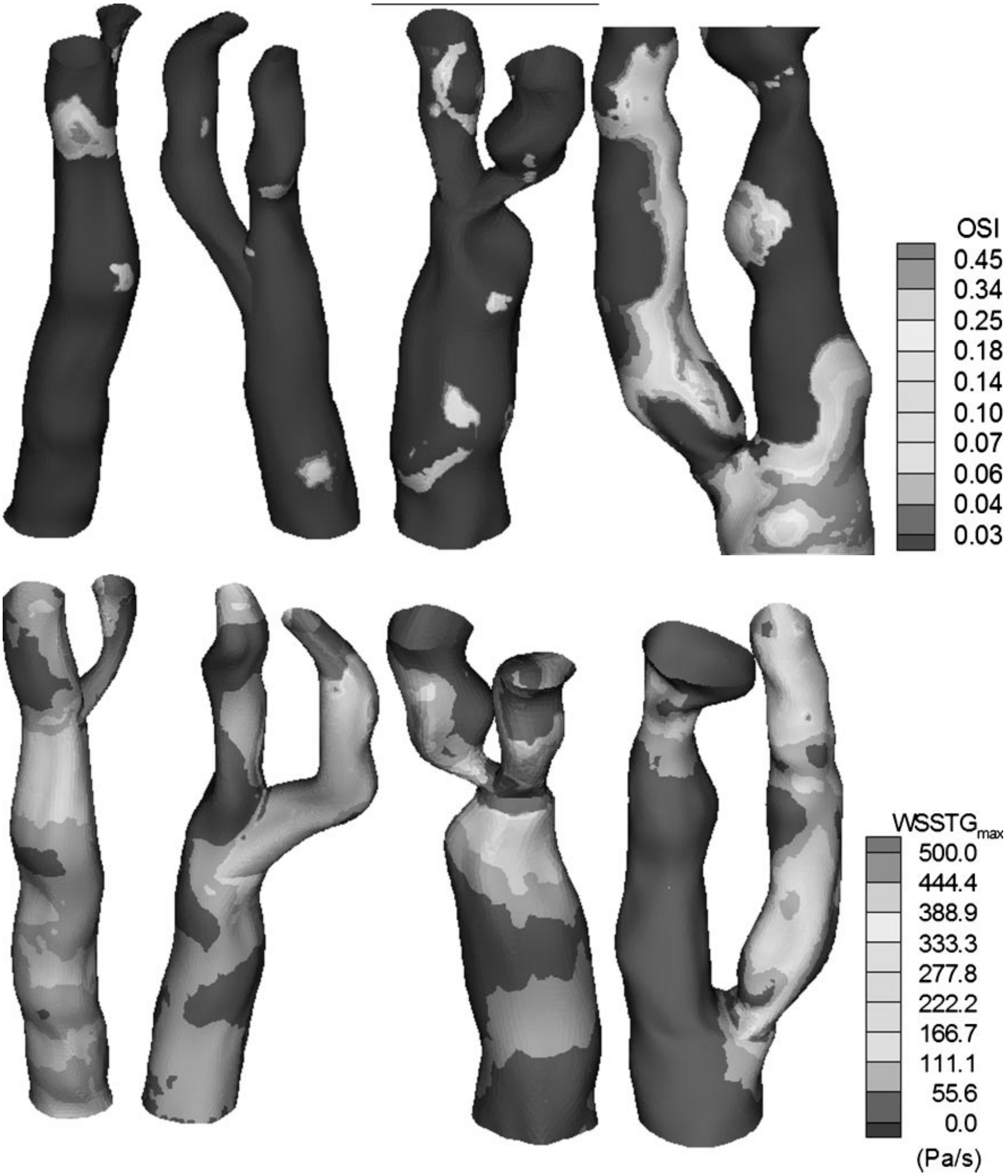

FIGURE 6. Continued.

throat of the stenoses in the internal carotid of P2 (values between 3 and 6 Pa) except at the flow divider, where high shear stress is expected.[24,28] Levels of shear stress increase again, however, at the outlet of the ECA of P2 at the site of another constriction. WSS levels in the CCA are quite uniform in all patients and hover around 1 Pa, except in P4, where the shear stress is lower. This may be due in part to the incomplete imaging of the CCA in P4 necessitating the application of the upstream boundary condition just proximal to the bifurcation. Pronounced areas of low wall shear stresses (and flow recirculation) are often found downstream of the stenoses in each of the patients. These also coincide with areas of high OSI in some of the patients (e.g., P1, in the vicinity of the carotid bulb, and several regions in P4). Another prominent region of low WSS is near the upstream edge of the carotid bulb of P4 extending into the CCA, which was not subjected to excessive remodeling in this particular patient. This gives an appearance reminiscent of WSS patterns found in the carotid bulb of healthy volunteers.[27]

OSI is generally small, being <0.04 over much of the wall with the exception of P4. The few pockets of elevated OSI tend to be located in regions just distal to a local narrowing and favor the outer wall. Note that the short CCA segment may influence results for P4. Also, flow rates are much higher in P4 than the other patients so that the pressure gradients during deceleration will be larger, which would also encourage flow reversal near the wall.

In most locations of the FEM models, the WSSTG distribution approximates that of WSS, but the range of values tends to be much larger with some values in excess of 4000 Pa/s. WSS and WSSTG are shown to follow almost identical trends, for example, in slice 5 of P2 [Fig. 7(a)]. However, this is not always the case [see e.g., slice 2 of P4, Fig. 7(b)]. These distinctions are important in considering the associations between hemodynamic and histological parameters.

Regression Analysis

Only the significant results (with $P < 0.05$ using Spearman correlations) are plotted in Fig. 8 and listed in Table I. Data from slice 6 of P2 were not used in the analysis given the relatively poor quality of the histological section. It is worth noting that essentially no significant correlations (3 out of 72 possible ones) were found for the data of P4. Of the 80 possible correlations (a total of 20 slices considered, each with four histological variables) between WSSTG and each of the four components, 30 were significant. For WSS, 31 of 80 possible correlations were significant, and for OSI, 15 of 80. Of those sections that yielded significant correlations, several trends are worth noting. First, in all cases, the correlations with WSSTG and WSS were always of the same sign, and the correlation with OSI was always of the opposite sign. That is, if WSS exhibited a positive correlation, then the correlation with WSSTG was also positive while the correlation with OSI was negative. Second, SMC and COL showed a tendency that was exactly opposite to that of LIP and Mϕ, for each of the hemodynamic parameters analyzed. That is, while SMC and COL were positively correlated with WSSTG and WSS and negatively correlated with OSI, all these trends were reversed for both LIP and Mϕ.

DISCUSSION

Overall Strategy

Most previous computational studies examining the relationship between hemodynamics and atherosclerosis have focused on early-stage disease in normal arterial geometries. With disease progression, however, localized wall thickening alters flow geometry and, consequently, the patterns of flow and wall shear stress. While it is generally thought that hemodynamics continue to play a role, we know little of the relationship between flow and the inflammatory process in the advanced lesion. Carotid endarterectomy therefore provides a unique opportunity to examine this relationship since the same diseased vessel can be viewed *in vivo*, then examined histologically following excision.

The local fluid dynamics is highly related to specifics of geometry and flow waveform, and the approximations necessary in a study such as this (e.g., imaging accuracy, segmentation, conversion to a numerical grid, smoothing operations, etc.) can greatly affect accuracy in the final CFD results. The authors are aware of these factors and attempt to address them, but the challenge in dealing with such distorted vessels is considerable.

The limited availability of subjects, coupled with the extent and subject-to-subject variability of the disease process (and hence the tortuous geometries with resultant sensitivity in the velocity field calculations), makes it difficult to draw any definitive conclusions about a relationship between hemodynamics and plaque composition. However, despite the limitations of this study that combines *in vivo* and *ex vivo* data, the developed methodology and the reported preliminary results demonstrate the feasibility and potential usefulness of this approach.

Hemodynamics of Advanced Lesions

Global flow patterns and also the detailed distribution of hemodynamic parameters were found to be grossly distorted by the changes in vessel geometry brought about by the disease process. To the extent that continued progression of the lesion results from the same hemodynamic conditions that initiated it, changes in the pattern of lesion growth should reflect these hemodynamic variations. The carotid bulb, for example, exhibits early atherogenic changes, and these often develop into advanced lesions with severe stenoses. Local narrowing of the artery, however, should lead to a subsequent *increase* in shear stress locally, and to the extent that increased shear is atheroprotective, this should slow disease progression there. We found evidence supporting the theory that the same relationships seen in atherogenesis are operative in advanced lesions as well. The carotid bulb is no longer a region of uniformly low shear stress, however; pockets of low shear *and high shear* can be found there, but their distributions differ dramatically between subjects.

All patients exhibited highly nonuniform distributions of WSS distal to the bifurcation. Simulations for P1 and P2, and to a lesser extent for P4, show pools of high WSS, reaching values in excess of 10 Pa, in the ECA at sudden constrictions downstream of the bifurcation. In P3, sudden constrictions associated with islands of high WSS, occur mostly at the bifurcation itself, and to a lesser extent downstream of the bifurcation. P1, P2, and P4 also show regions

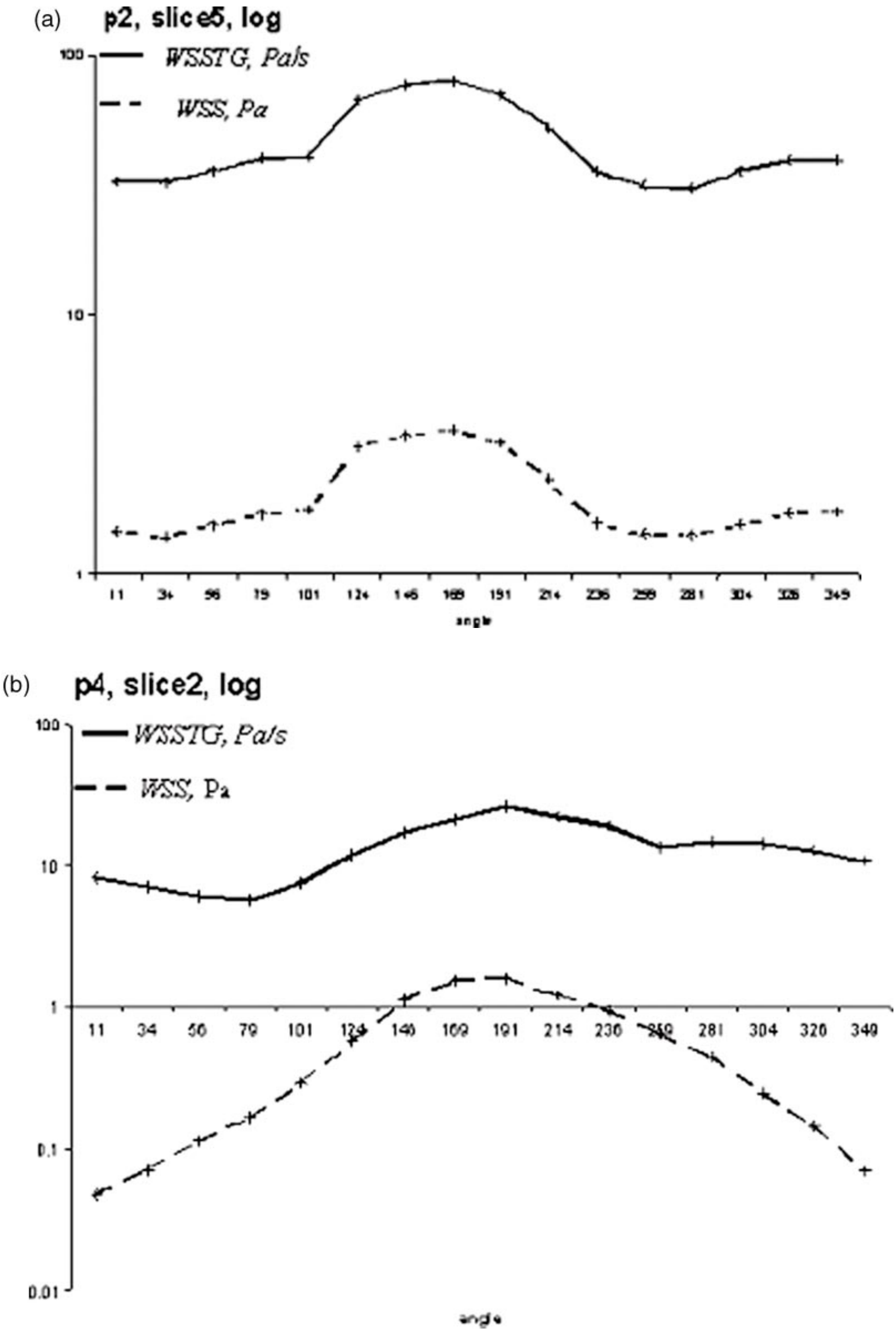

FIGURE 7. (a) Logarithmic plot of WSS and WSSTG as a function of angle for P2, slice 5. (b) Logarithmic plot of WSS and WSSTG as a function of angle for P4, slice 2. Both WSS and WSSTG values are obtained by taking the average per 22.5° segments (and 1 mm thickness; 0.5 mm above and 0.5 mm below the selected cutting plane) of values resulting from the FEM simulation. The angle is measured counterclockwise (when viewing the FEM cutting plane from the distal direction); 0° is diametrically opposite to the flow divider in the internal carotid, at the surgical incision.

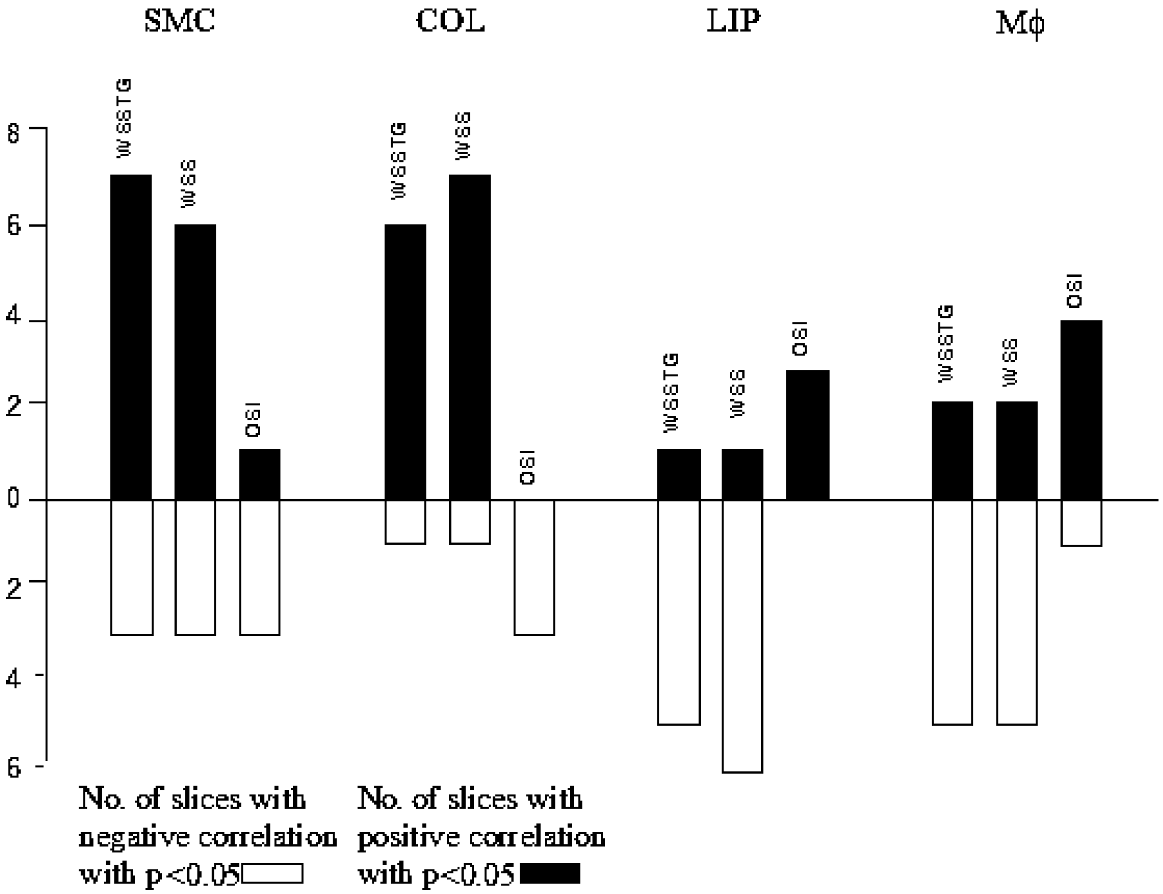

FIGURE 8. Summary bar graph of the number and sign of correlations of histology data (SMC, Mϕ, COL, and LIP) to hemodynamic data (WSSTG, WSS, and OSI). The Spearman rank order correlation coefficient and its corresponding significant test were used in evaluating the correlations between each pair of variables (one hemodynamic parameter and one chemical component, respectively). These correlations were studied circumferentially, for a particular axial position z, as a function of angle θ. There are 16 data points per slice, and only those correlations with $p < 0.05$ were considered conclusive (for the purpose of the regression analysis of this study, P values were rounded off to 2 decimal places). Positive correlations are shaded in black; negative correlations are shown in white.

of low WSS (≤0.1 Pa) at the ICA distal to the bifurcation opposite the flow divider, at the carotid bulb location. In the case of P4, this pool extends almost completely around the circumference of the internal carotid. The sudden constrictions found immediately distal to the bifurcation in P3, overlapping the carotid bulb, could explain the absence of a low wall shear stress pool in this patient at this location. In P3 and P4, pools of low WSS are also found upstream of the bifurcation. This occurs at regions where the vessel has expanded, perhaps in response to constrictions that have developed downstream. We note that only a small portion of the CCA of P4 was imaged, as compared to the other patients where regions both distal and proximal to the bifurcation were imaged.

The magnitude of circumferential variability in WSS at a particular axial position changes according to axial location and local geometry. For example, in P1, WSS varies between 1.2 and 1.7 Pa in slice 3 (just proximal to the bifurcation), while values range between 1.5 and 21.3 Pa in slice 4 (just distal to the bifurcation). This illustrates how the relative lack of variation in certain slices may adversely affect our ability to discern correlations, and likely contributes to the relative absence of significant correlations proximal to the bifurcation.

Downstream of a stenosis, pressure recovery and the wall curvature associated with the increase in cross-sectional area give rise to flow separation. Flow reversal occurs primarily near the boundaries of the separation zone where the flow is most likely to reverse direction as the reattachment line moves back-and-forth due to temporal variations in flow rate. Accordingly, pools of high OSI are observed in all patients, typically at the edge of the low shear stress regions.

Trends in the Preliminary Data

Previous work has shown that in the late stages of atherosclerosis, low or oscillatory fluid shear stress

TABLE 1. Spearman correlation coefficient ρ, and P value for significant correlations ($P < 0.05$). For the purpose of the regression analysis of this study, P values were rounded off to 2 decimal places.

	SMC and WSSTG			SMC and WSS			SMC and OSI	
	ρ	P value		ρ	P value		ρ	P value
P1, slice3	0.6000	0.0140	P1, slice3	0.5235	0.0374	P1, slice5	−0.6409	0.0075
P1, slice5	0.5147	0.0413	P1, slice5	0.5765	0.0194	P2, slice4	−0.6016	0.0137
P2, slice1	0.6269	0.0093	P2, slice1	0.6180	0.0107	P3, slice1	0.6115	0.0118
P2, slice2	−0.5529	0.0263	P2, slice2	−0.6265	0.0094	P4, slice2	−0.6601	0.0054
P2, slice3	0.5265	0.0362	P2, slice4	0.6676	0.0047			
P2, slice4	0.6765	0.0040	P3, slice1	−0.6176	0.0108			
P3, slice1	−0.6765	0.0040	P3, slice3	0.6412	0.0074			
P3, slice3	0.6706	0.0045	P3, slice4	−0.5500	0.0273			
P3, slice4	−0.6176	0.0108	P4, slice2	0.6176	0.0108			
P4, slice2	0.6265	0.0094						
	LIP and WSSTG			LIP and WSS			LIP and OSI	
P1, slice1	−0.6412	0.0074	P1, slice1	−0.6088	0.0123	P1, slice4	0.5634	0.0230
P1, slice3	−0.5676	0.0218	P1, slice3	−0.5176	0.0400	P1, slice5	0.8074	0.0002
P1, slice5	−0.8265	0.0001	P1, slice4	−0.5294	0.0350	P3, slice1	0.6401	0.0076
P2, slice1	0.8329	0.0001	P1, slice5	−0.8647	0.0000			
P3, slice3	−0.5971	0.0146	P2, slice1	0.8090	0.0001			
P3, slice4	−0.7912	0.0003	P3, slice3	−0.5912	0.0159			
			P3, slice4	−0.7324	0.0013			
	Mϕ and WSSTG			Mϕ and WSS			Mϕ and OSI	
P1, slice4	−0.7294	0.0013	P1, slice4	−0.7853	0.0003	P1, slice3	0.4985	0.0494
P2, slice1	0.7672	0.0005	P2, slice1	0.7464	0.0009	P1, slice4	0.5487	0.0277
P2, slice3	−0.7059	0.0022	P2, slice3	−0.5265	0.0362	P2, slice4	0.7503	0.0008
P2, slice4	−0.8353	0.0001	P2, slice4	−0.8294	0.0001	P3, slice1	−0.5364	0.0322
P3, slice1	0.7000	0.0025	P3, slice1	0.6441	0.0071	P3, slice3	0.5028	0.0471
P3, slice3	−0.5706	0.0210	P3, slice2	−0.6412	0.0074			
P3, slice4	−0.6824	0.0036	P3, slice4	−0.6176	0.0108			
	COL and WSSTG			COL and WSS			COL and OSI	
P1, slice3	−0.7559	0.0007	P1, slice1	0.4941	0.0517	P1, slice5	−0.5278	0.0356
P1, slice4	0.5059	0.0456	P1, slice3	−0.5471	0.0283	P2, slice1	−0.6298	0.0089
P1, slice5	0.5500	0.0273	P1, slice4	0.5235	0.0374	P2, slice4	−0.8500	0.0000
P2, slice1	0.6018	0.0137	P1, slice5	0.5559	0.0254			
P2, slice4	0.7353	0.0012	P2, slice1	0.6417	0.0074			
P2, slice5	0.5471	0.0283	P2, slice4	0.7735	0.0004			
P3, slice4	0.7082	0.0021	P2, slice5	0.6088	0.0123			
			P3, slice4	0.6785	0.0039			

correlates with vulnerable areas in the atherosclerotic plaque, such as sites with significant lipid deposition,[8] and macrophage accumulation.[22] These findings agree with the observed trend of both LIP and Mϕ correlating negatively with WSS and WSSTG and positively with OSI. Similarly, Sukhova *et al.*[33] found that vulnerable areas in the atherosclerotic plaque have increased collagenolysis (decreased COL), and Falk[12] have shown that fibrous caps that have ruptured have not only twice as many macrophages as unruptured fibrous caps but also half as many smooth muscle cells. This decreased COL and SMC content relative to Mϕ and LIP, which correlates with plaque vulnerability and low or oscillatory fluid shear stress, is in agreement with the observed trend of both COL and SMC correlating positively with WSS and WSSTG and negatively with OSI. These results, though encouraging, need to be tempered by the fact that, in some cases, more than 75% of the slices exhibited no significant correlation.

Methodological Considerations: Imaging

Image accuracy is critical to the CFD model. Angiography on the patients was not available at the time of the study. If angiography had been available to us, once the 3D reconstruction was done, it would have been useful to compare the reconstructed image model directly to the angiographic images.

While difficult to assess, the assumption of Womersley flow based on centerline velocities is a source of error, especially in the ICA or ECA outlets, due to the secondary flows likely to exist at these locations. It would have been preferable to use MR phase contrast to better define the velocity profiles, but at the time that the study was performed, this would have led to an unacceptably long scan time for the patients. Indeed, from the methodological viewpoint, this would have been vastly superior to using Womersley theory in the FEM simulations.

It is worth noting that very few correlations were found in patient P4. This can be explained by the fact that only a short segment of CCA was imaged, and hence the imposed boundary conditions of fully developed Womersley flow at the inlet plane almost certainly do not apply. Similarly, P4 has an unusually high CCA flow rate. The hemodynamic map for this patient might therefore be inaccurate and possibly explain the lack of correlations with histological parameters

Methodological Considerations: Finite Element Modeling

Inaccuracies would arise in the FEM simulations if the flow were turbulent, since laminar flow was assumed. Turbulence would, in fact, be more likely to occur in these diseased geometries and should therefore be considered in future studies. Either ultrasound or MR can be used, not to quantify the turbulence, but at least to indicate its presence.

Another limitation of this study is that the arterial walls were assumed rigid. Although such assumption is believed to minimally influence the flow patterns in diseased, stiffened arteries, detailed assessment of compliant walls merits a fluid-structure interaction study in the future.

Although the main focus of the present study was to investigate possible correlations between fluid dynamic parameters and histological factors, the multifactorial nature of atherosclerosis merits further examination of wall mechanic parameters as well while the link between mechanical patterns and atherosclerosis is sought.

Correlations were attempted using WSS, WSSTG, and OSI. WSS is a derivative of the primary variables being calculated (i.e., velocity) and hence may be more subject to error than the velocity itself. WSSTG is a derivative of the WSS, which may lead to further errors. This, coupled with uncertainties in geometry and velocity profile boundary conditions, leads to a fair degree of uncertainty in these hemodynamic variables, pointing to the need for extra caution in drawing strong conclusions.

OSI as defined in Eq. (1) is a rough measure of changes in direction of the WSS vector during the cycle. The *in vitro* model used by Ku *et al*. had a plane of symmetry, and the definition was based on actual local WSS reversal at the walls along this plane. In the case of a “real” carotid bifurcation, the geometry is strongly nonplanar, and local WSS vectors may change considerably in angular orientation during the cycle, not just in the sense of forward or reverse direction. Hence, the OSI is a somewhat arbitrary index of WSS vector orientation changes in 3D flows and potentially less useful. It is not surprising that significant correlations between this variable and biological markers of disease were less numerous than those found in the cases of WSS and WSSTG. It is worth noting, that our results do not to imply that WSS directional variation is not important in development of arterial disease, but that the definition of OSI chosen for this study is not optimal for a real carotid bifurcation geometry.

Methodological Considerations: Regression Analysis

While trends in these preliminary data are generally in the anticipated directions, there are exceptions, and these might be attributable to several factors: (i) differences in the stage of disease progression at different plaque locations, (ii) subject-to-subject variability, or (iii) changes in local flow state occurred as a result of disease progression and arterial remodeling.

Errors in registration on the order of 1 mm between the histological and FEM cross-sections are also possible. Although errors of this magnitude would have little effect elsewhere, they would be more problematic in the immediate vicinity of a stenosis where cross-sectional shape and area are undergoing a rapid change.

A contributing factor to registration error is the uncertainty in the location of the cut performed at the time of surgery, which is assumed to be diametrally opposed to the flow divider along the ICA at all axial locations. A current measure introduced to reduce these errors, is to embed the specimen in a gel, with reference markers spanning the length of the plaque, and photographing the excised specimens prior to cutting and staining.

Concluding Remarks

This study describes a promising noninvasive method for evaluating atherosclerosis progression, which could eventually lead to the development of an index of plaque vulnerability to be used in the diagnosis and decision-making processes regarding patients with different degrees of atherosclerotic progression.

Considerable potential exists to advance our understanding of the relationship between hemodynamics and advanced atherosclerotic disease using the methods described here. The opportunity to routinely obtain *in vivo* images and histology from the same lesion, however, may soon disappear due to the growing movement to abandon endarterectomy in favor of stenting in combination with embolic protection devices. Given the strong likelihood that carotid stenting will eventually replace endarterectomy, it is critical that research on excised noncadaveric carotid plaque specimens, such as that discussed in this paper, takes place in the next few years, prior to this transition taking place.

ACKNOWLEDGMENTS

Support from the National Heart, Lung, and Blood Institute (HL 61794), and technical assistance from A. H.

Chau, L. V. Contreras, L. A. Kim, T. S. Kim, S. G. Reddy, D. Santhumayor, C. P. Thai, and C. K. Yang are gratefully acknowledged.

REFERENCES

[1]AHA. 1998 Heart and Stroke Statistical Update. Dallas, TX: American Heart Association, 1997.

[2]Berger, S. A., and L. D. Jou. Flows in stenotic vessels. *Ann. Rev. Fluid Mech.* 32:347–384, 2000.

[3]Bonnet, A. Characterization of global minimizers for Mumford-Shah functional image segmentation. *Comptes Rendus de l'Academie des Sciences, Serie l-Mathematique* 321:1121–1126, 1995.

[4]Chan, R. C., J. Kaufhold, R. Lees, and W. Karl. Ultrasound analysis of vascular structure and deformation. In: SPIE, Aerosense 2000, edited by H. H. Pien. Orlando, FL: Battlefield Biomedical Technologies II, 2000, pp. 24–28.

[5]Davies, P. F. Endothelial cells, hemodynamic forces, and the localization of atherosclerosis. In: Endothelial Cells. Boca Raton, FL: CRC Press, 1988.

[6]Davies, P. F., and S. C. Tripathi. Mechanical-stress mechanisms and the cell—An endothelial paradigm. *Circ. Res.* 72:239–245, 1993.

[7]Delfino, A., N. Stergiopulos, J. E. Moore, Jr., and J. J. Meister. Residual strain effects on the stress field in a thick wall finite element model of the human carotid bifurcation. *J. Biomech.* 30:777–786, 1997.

[8]Deng, X. Y., P. W. Stroman, and R. Guidoin. Theoretical modeling of the release rate of low-density lipoproteins and their breakdown products at arterial stenoses. *Clin. Invest. Med.* 19:83–91, 1996.

[9]Dirksen, M. T., A. C. van der Wal, F. M. van den Berg, C. M. van der Loos, and A. E. Becker. Distribution of inflammatory cells in atherosclerotic plaques relates to the direction of flow. *Circulation* 98:2000–2003, 1998.

[10]Edelman, R. R., D. Chien, and D. Kim. Fast selective black blood MR imaging. *Radiology* 181:655–660, 1991.

[11]Ethier, C. R. Computational modeling of mass transfer and links to atherosclerosis. *Ann. Biomed. Eng.* 30:461–471, 2002.

[12]Falk, E. Progressive atherogenesis: Why do plaques rupture. *Circulation* 86:lll-30–lll-42, 1992.

[13]Gonzales, R. S., and T. M. Wick. Hemodynamic modulation of monocytic cell adherence to vascular endothelium. *Ann. Biomed. Eng.* 24:382–393, 1996.

[14]He, X., D. N. Ku, and J. E. Moore, Jr. Simple calculation of the velocity profiles for pulsatile flow in a blood vessel using Mathematica [published erratum appears in *Ann. Biomed. Eng.* 21(5):557–558, 1993]. *Ann. Biomed. Eng.* 21:45–49, 1993.

[15]Kaazempur-Mofrad, M., and C. Ethier. Mass transport in a Realistic Human Right Coronary Artery Model. *Ann. Biomed. Eng.* 29:121–127, 2001.

[16]Kaazempur-Mofrad, M. R., M. Bathe, H. Karcher, H. Younis, H. Seong, E. Shim, R. Chan, D. Hinton, M. Powers, L. Griffith, and R. Kamm. Role of simulation in understanding biological systems. *Comput. Struct.* 81:715–726, 2003.

[17]Kaazempur-Mofrad, M. R., H. F. Younis, S. Patel, A. G. Isasi, C. Chung, R. C. Chan, D. P. Hinton, R. T. Lee, and R. D. Kamm. Cyclic strain in human carotid bifurcation and its potential correlation to atherogenesis: Idealized and anatomically-realistic models. *J. Eng. Math.* 47:299–314, 2003.

[18]Klein, A. K., F. Lee, and A. A. Amini. Quantitative coronary angiography with deformable spline models. *IEEE Trans. Med. Imaging* 16:468–482, 1997.

[19]Ku, D. Blood flow in arteries. *Ann. Rev. Fluid Mech.* 32:346–384, 1997.

[20]Ku, D. N., D. P. Giddens, C. K. Zarins, and S. Glagov. Pulsatile flow and atherosclerosis in the human carotid bifurcation. Positive correlation between plaque location and low oscillating shear stress. *Arteriosclerosis* 5:293–302, 1985.

[21]Lee, R. T., F. J. Schoen, H. M. Loree, M. W. Lark, and P. Libby. Circumferential stress and matrix metalloproteinase 1 in human coronary atherosclerosis. Implications for plaque rupture. *Arterioscler. Thromb. Vasc. Biol.* 16:1070–1073, 1996.

[22]Libby, P., Y. J. Geng, M. Aikawa, U. Schoenbeck, F. Mach, S. K. Clinton, G. K. Sukhova, and R. T. Lee. Macrophages and atherosclerotic plaque stability. *Curr. Opin. Lipidol.* 7:330–335, 1996.

[23]Malek, A. M., S. L. Alper, and S. Izumo. Hemodynamic shear stress and its role in atherosclerosis. *JAMA* 282:2035–2042., 1999.

[24]Milner, J. S., J. A. Moore, B. K. Rutt, and D. A. Steinman. Hemodynamics of human carotid artery bifurcations: Computational studies with models reconstructed from magnetic resonance imaging of normal subjects. *J. Vasc. Surg.* 28:143–156, 1998.

[25]Mohan, S., N. Mohan, and E. A. Sprague. Differential activation of NF-kappa B in human aortic endothelial cells conditioned to specific flow environments. *Am. J. Physiol.* 273:C572–C578, 1997.

[26]Moore J. A., B. Rutt, S. J. Karlik, K. Yin, and C. R. Ethier. Computational blood flow modeling based on *in vivo* measurements. *Ann. Biomed. Eng.* 27:627–640, 1999.

[27]Perktold, K., and G. Rappitsch. Computer simulation of local blood flow and vessel mechanics in a compliant carotid artery bifurcation model. *J. Biomech.* 28:845–856, 1995.

[28]Perktold, K., M. Resch, and H. Florian. Pulsatile non-Newtonian flow characteristics in a three-dimensional human carotid bifurcation model. *J. Biomech. Eng.* 113:464–475, 1991.

[29]Rosner, R. A. *Regression and Correlation Methods.* Boston, MA: PWS Publishers, 1986.

[30]Simonetti, O. P., J. P. Finn, R. D. White, G. Laub, and D. A. Henry. "Black blood" T2-weighted inversion-recovery MR imaging of the heart. *Radiology* 199:49–57, 1996.

[31]Steinman, D. A., J. B. Thomas, H. M. Ladak, J. S. Milner, B. K. Rutt, and J. D. Spence. Reconstruction of carotid bifurcation hemodynamics and wall thickness using computational fluid dynamics and MRI. *Magn. Reson. Med.* 47:149–159, 2002.

[32]Stroud, J. S. Numerical Simulations of Blood Flow in Stenotic Vessels, PhD dissertation, University of California at Berkeley, Berkeley, 2000.

[33]Sukhova, G. K., U. Schonbeck, E. Rabkin, F. J. Schoen, A. R. Poole, R. C. Billinghurst, and P. Libby. Evidence for increased collagenolysis by interstitial collagenases-1 and -3 in vulnerable human atheromatous plaques. *Circulation* 19:2503–2509, 1999.

[34]Sumpio, B. E. Hemodynamic forces and the biology of the endothelium—Signal transduction pathways in endothelial-cells subjected to physical forces *in vitro*. *J. Vasc. Surg.* 13:744–746, 1991.

[35]Tarbell, J. Mass transport in arteries and the localization of atheroslerosis. *Ann. Rev. Biomed. Eng.* 5:79–118, 2003.

[36]Thoumine, O., R. M. Nerem, and P. R. Girard. Changes in organization and composition of the extracellular-matrix, underlying cultured endothelial-cells exposed to laminar steady shear-stress. *Lab. Invest.* 73:565–576, 1995.

[37]Tsao, P. S., R. Buitrago, J. R. Chan, and J. P. Cooke. Fluid flow inhibits endothelial adhesiveness. Nitric oxide and

transcriptional regulation of VCAM-1. *Circulation* 94:1682–1689, 1996.

[38] Tsao, P. S., N. P. Lewis, S. Alpert, and J. P. Cooke. Exposure to shear stress alters endothelial adhesiveness. Role of nitric oxide. *Circulation* 92:3513–3519, 1995.

[39] Williamson, S. D., Y. Lam, H. F. Younis, S. Patel, M. R. Kaazempur-Mofrad, and R. D. Kamm. On the sensitivity of wall stresses in diseased arteries to variable material properties. *J. Biomech. Eng* 125:147–155, 2003.

[40] Zhao, S. Z., X. Y. Xu, M. W. Collins, A. V. Stanton, A. D. Hughes, and S. A. Thom. Flow in carotid bifurcations: Effect of the superior thyroid artery. *Med. Eng. Phys.* 21:207–214, 1999.

[41] Zwiebel, W. J. Peripheral vascular system. *Ultrasound Med. Biol.* 26:S92–S96, 2000.